Rapidly rotating spherical Couette flow in a dipolar magnetic field: an experimental study of the mean axisymmetric flow

Henri-Claude Nataf, Thierry Alboussiere, Daniel Brito, Philippe Cardin, Nadège Gagnière, Dominique Jault, Denys Schmitt

Rapidly rotating spherical Couette flow in a dipolar magnetic field: an experimental study of the mean axisymmetric flow

Nataf, H.-C. * Alboussière, T., Brito, D., Cardin, P., Gagnière, N., Jault, D., and Schmitt, D.

Geodynamo team, LGIT-UMR5559-CNRS-UJF, Grenoble, France

Abstract

In order to explore the magnetostrophic regime expected for planetary cores, in which the Lorentz forces balance the Coriolis forces, experiments have been conducted in a rotating sphere filled with liquid sodium, with an imposed dipolar magnetic field (the *DTS* setup). The field is produced by a permanent magnet enclosed in an inner sphere, which can rotate at a separate rate, producing a spherical Couette flow. The flow properties are investigated by measuring electric potentials on the outer sphere, the induced magnetic field in the laboratory frame just above the rotating outer sphere, and velocity profiles inside the liquid sodium using ultrasonic Doppler velocimetry. The present article focuses on the mean axisymmetric part of the flow. The electric potential differences measured at several latitudes can be linked to azimuthal velocities, and are indeed found to be proportional to the azimuthal velocities measured by Doppler velocimetry. The Doppler profiles show that the angular velocity of the fluid is relatively uniform in most of the fluid shell, but rises near the inner sphere, revealing the presence of a "magnetic wind". We show that the measured electric potential difference can be used as a proxy of the actual fluid velocity. Using this proxy in place of the imposed differential velocity, we find that the induced magnetic field varies in a consistent fashion, and displays a peculiar peak in the counter–rotating regime. This happens when the fluid rotation rate is almost equal and opposite to the outer sphere rotation rate. The fluid is then almost at rest in the laboratory frame, and the Proudman–Taylor constraint vanishes, enabling a strong meridional flow. We suggest that dynamo action might be favored in such a situation.

Key words: Spherical Couette flow, magnetostrophic, liquid sodium experiment, dynamo, ultrasonic Doppler velocimetry.
PACS: 47, 47.65, 91, 91.25

1 Introduction

The internal dynamics of the liquid core of the planets is deeply influenced by the rotation of the planet and (in many cases) by the presence of a magnetic field, and can be in the so–called magnetostrophic regime. In recent years, attention has been paid to the rotating spherical Couette flow in the presence of a magnetic field (Kleeorin et al., 1997; Hollerbach, 1994; Dormy et al., 1998; Starchenko, 1998; Hollerbach, 2000; Nataf et al., 2006). An electrically conducting liquid fills the gap between two concentric spheres and is sheared through the differential rotation of the two spheres. A magnetic field can be applied. This flow has the distinct advantage of being amenable to both experiments and numerical models, while retaining important ingredients of natural situations. Numerical simulations (Dormy et al., 1998; Hollerbach, 2000) and asymptotics (Kleeorin et al., 1997; Starchenko, 1998; Dormy et al., 2002) highlight the importance of the magnetic wind that arises when the magnetic field lines are not parallel to the rotation axis, as for a dipolar field. This magnetic wind can entrain the fluid at angular velocities larger than that of the inner sphere, a phenomenon called super–rotation (Dormy et al., 1998, 2002). The rotating spherical Couette flow has also been proposed for producing a dynamo (Cardin et al., 2002). Numerical models have shown that dynamo action could be produced this way, even in liquids with a low magnetic Prandtl number, such as liquid metals (Schaeffer & Cardin, 2006). This has led Dan Lathrop and his team to build a 3m–diameter sphere with a rotating inner sphere in the hope of starting a dynamo, once the gap is filled with liquid sodium and the differential rotation is large enough.

Here, we report on results obtained in the *DTS* (*Derviche Tourneur Sodium*) experiment. This experiment, described in Cardin et al. (2002) and Nataf et al. (2006), is a rotating spherical Couette flow with an imposed axisymmetric dipolar magnetic field. Because of this strong imposed field, and although liquid sodium is used, *DTS* is not a dynamo experiment. However, it permits to explore very similar dynamics. In particular, the magnetic field is large enough to strongly influence the flow (interaction parameter N up to 200) and the magnetic field is strongly affected by the flow (magnetic Reynolds number Rm up to 44).

This kind of experiment can bring information on the level and organization of turbulence in situations where both rotation and the magnetic field impose strong constraints on the flow. Local theories have been proposed (Braginsky

* corresponding author
Email address: Henri-Claude.Nataf@ujf-grenoble.fr (Nataf, H.-C.).
URL:
http://www-lgit.obs.ujf-grenoble.fr/recherche/geodynamo/Epage.html
(Nataf, H.-C.).

& Meytlis, 1990), partly backed by numerical simulations (St. Pierre, 1996), and some teams are trying to implement sub-grid models based on these theories in full dynamo models (Buffett, 2003; Matsui & Buffett, 2006). Results obtained in the DTS experiment suggest an alternative view, in which waves play a major role (Schmitt et al., 2007). A good characterization of the mean axisymmetric flow is needed in order to fully exploit these observations.

An experimental setup, built by Dan Lathrop and his group (Sisan et al., 2004; Kelley et al., 2007) is very similar to our DTS experiment. The main difference is that an axial magnetic field is applied by external coils in Sisan et al. (2004) and Kelley et al. (2007), while we impose a strong dipolar magnetic field in DTS since the inner sphere contains a permanent magnet. One of the consequences is that the entrainment of the conducting fluid is much stronger, since the inner sphere acts as a magnetic stirrer. We also have developed specific instrumentation, such as measuring the electric potential at the surface of the outer sphere, which carries important information on the flow (Nataf et al., 2006; Schmitt et al., 2007).

In this article, we focus on the mean axisymmetric magnetohydrodynamic flow observed in DTS when the outer sphere rotates. The first observations were described in Nataf et al. (2006), and more thorough results for a static outer sphere will be discussed in a forthcoming article (Brito et al., 2007).

Nataf et al. (2006) showed that the measurement of electric potential differences at the surface of the outer sphere could be related to the azimuthal velocity of the liquid beyond the Hartmann boundary layer. It was found that this velocity could be larger than the solid-body rotation of the inner sphere, providing experimental evidence for the so-called super-rotation predicted by Dormy et al. (1998). However, the latitudinal variation of the electric potential differences was found to differ markedly from the one calculated in a linear numerical model, analogous to that of Dormy et al. (1998). The relative variation of electric potential differences with latitude turned out to be universal, independent of the differential rotation of the inner sphere. This was particularly true when the outer sphere was at rest. The electric design of the electrodes and acquisition system has been improved since, yielding better quality signals, and we will show in this article that the situation is more complex when the outer sphere is rotating.

Direct measurements of the flow velocity were presented in Nataf et al. (2006), using ultrasonic Doppler velocimetry, but only radial profiles of the radial velocity could be obtained. The setup now permits the record of profiles of the azimuthal velocity as well, revealing the actual variation of azimuthal velocity inside the sphere. The profiles demonstrate that the distribution of azimuthal velocity differs markedly from solid-body rotation. In this article, we examine the characteristics of the profiles when global rotation is present.

In order to explain the difference between the observed and predicted latitudinal variation of electric potential differences, Nataf et al. (2006) suggested that the crescent of super–rotation was pushed away from the inner sphere toward the outer sphere by the centrifugal flow. We will see that the velocity profiles do not support this view. On the contrary, we show that the zone of large rotation moves closer to the inner sphere when differential rotation increases. Non–linear numerical computations reveal the same behavior (Hollerbach et al., 2007; Cardin & Jault, 2007). One example is shown in figure 1, which displays contours of the adimensional angular velocity for a particular simulation. This simulation was chosen because it yields velocity profiles that resemble the experimental ones, although the parameter ranges are rather different. Near the inner sphere, a strong magnetic wind entrains the fluid to a maximum angular velocity that reaches 1.19 times that of the inner sphere. For larger cylindrical radius, the constraint due the rotation of the outer sphere prevails, and the flow is geostrophic. We will show that the signature of these different regions are well observed in our experimental velocity profiles, although quantitative differences remain.

There were some hints in Nataf et al. (2006) that different flows could be observed for the same imposed velocities. With additional data now available, this tendency is fully confirmed. We think that this is due to variations in the electric coupling between the liquid sodium and the copper inner sphere. We show in this article that we can use the difference in electric potentials at one latitude (40° for example) as a proxy of the actual differential angular velocity of the fluid, and get a much more coherent picture of the various observations, if we relate them to this actual value.

No measurement of the induced magnetic field was provided by Nataf et al. (2006). We have not got yet an array of magnetometers, such as used by Kelley et al. (2006) to map inertial modes, but we measure the radial and orthoradial components of the induced magnetic field at a latitude of about 50° just outside the outer sphere, in the laboratory frame. The mean values correspond to the field induced by the mean meridional flow. When the outer sphere is rotating, a very peculiar behavior is monitored for a particular counter-rotation rate of the inner sphere.

We recall the main features of the DTS setup and measuring techniques in section 2. The typical dimensionless numbers are discussed in section 3. The results are presented in section 4, and discussed in section 5.

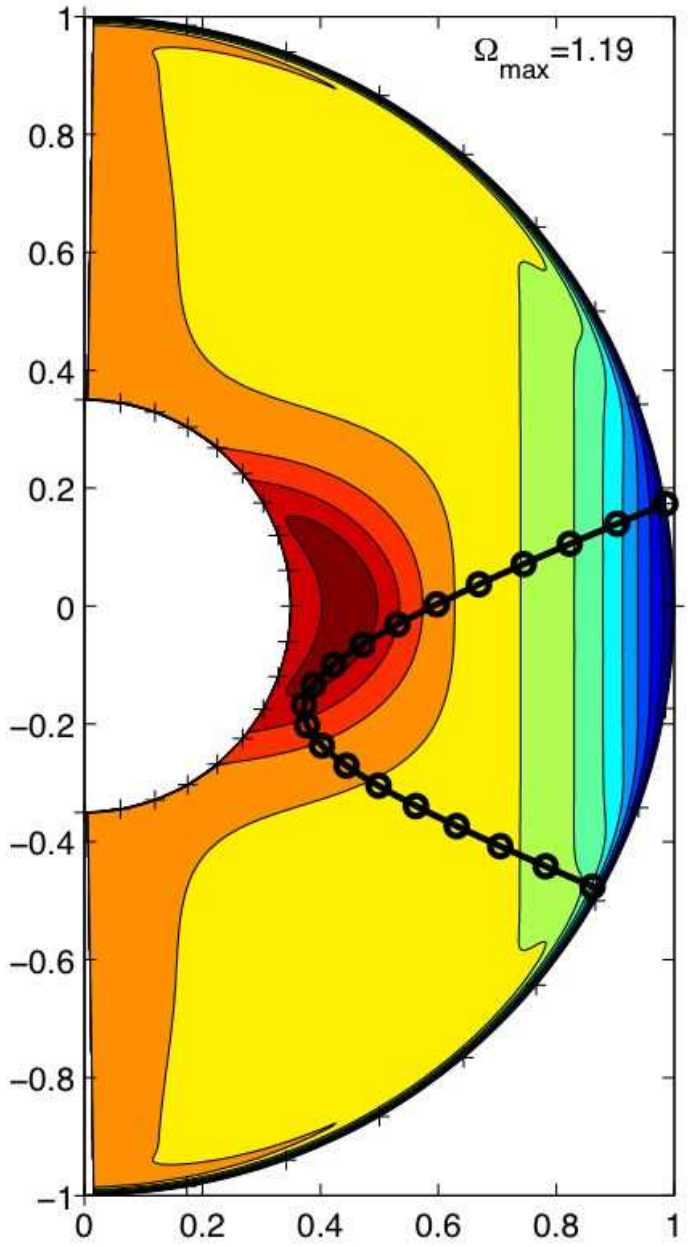

Fig. 1. Contour map of the angular velocity in a non–linear numerical simulation. The interval between contours is 10% of the angular velocity of the inner sphere. The dimensionless numbers (see section 3 below) for this simulation are: E = 10^{-4}, Re = 3000, $Pm = 10^{-4}$, and $Ha = 31.6$. Also drawn, the equivalent ray path of the ultrasonic beam shot from the "azimuthal" assembly at +10°, assuming axisymmetry. Marks are drawn every 2 cm along the ray path.

2 Experimental setup and measuring techniques

2.1 Setup

The central part of the DTS experiment is sketched in figure 2. Forty liters of liquid sodium are contained between a $b = 7.4$ cm–radius inner sphere and a $a = 21$ cm–radius outer spherical surface. The 5 mm–thick outer sphere is made of stainless steel, which is 8 times less conductive than sodium at 130°C, the typical experimental temperature. The inner sphere is made of two hollow copper hemispheres filled with 5 layers of magnetized rare-earth cobalt bricks. Outside the copper sphere, the magnetic field is found to be an axial dipole, aligned with the axis of rotation and pointing downwards with:

$$\vec{B}(r,\theta) = \frac{\mu_0 \mathcal{M}}{4\pi r^3}(2\vec{e}_r \cos\theta + \vec{e}_\theta \sin\theta)$$

in spherical coordinates, with θ the colatitude and $\mathcal{M} = -700$ Am^2 the magnetic dipolar moment, yielding a magnetic field amplitude ranging from 0.345 T at the poles of the inner sphere down to 0.008 T at the equator of the outer sphere. More details are given in Nataf et al. (2006).

The inner and outer spheres are set in rotation around the vertical axis. In this article, we present results obtained for imposed rotation rates f of the outer sphere of 5, 10 and 15 Hz. The rotation rate of the inner sphere in the laboratory frame is varied between -25 and +25 Hz, yielding differential rotation rates Δf of the inner sphere in the rotating frame ranging from -40 to 20 Hz (depending upon f). Each sphere is entrained by an 11 kW brushless electric motor (Yaskawa SGMGH-1ADCA61).

The torques and actual rotation rates are retrieved as analog signals from the two motor controllers. In order to decipher the organisation of the flow in the liquid, several techniques are employed. Electric potentials are measured at several locations on the outer sphere. Profiles of the flow velocity are obtained using ultrasonic Doppler velocimetry. Since the outer sphere is rotating, all these signals must pass through electric slip-rings to be analyzed in the laboratory frame. We use a 36–tracks 10A slip–ring system (Litton AC6275–12). In order to decrease electromagnetic perturbations of the signals, this system is completely enclosed in an aluminum casing. In contrast, the magnetic field is measured in the laboratory frame, with magnetometer sensors a few millimeters away from the rotating surface of the outer sphere.

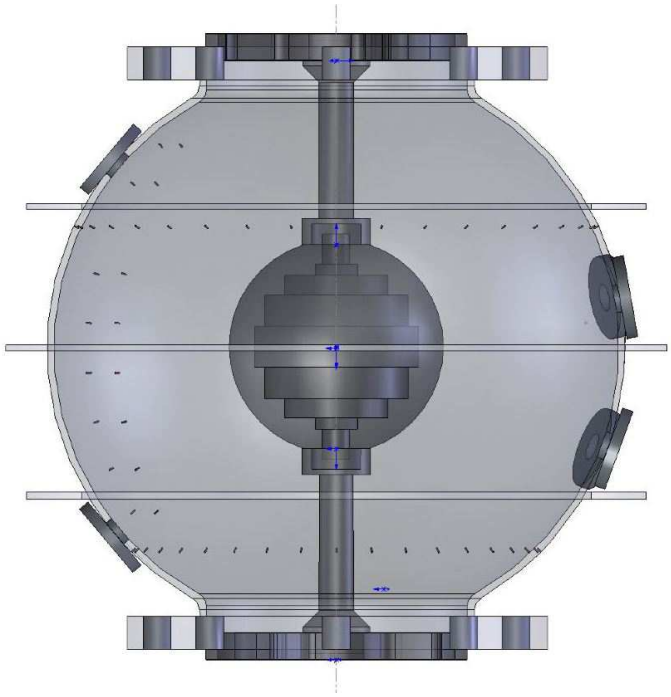

Fig. 2. Sketch of the central part of the *DTS* experiment. The 7.4 cm-radius inner sphere is made of copper and contains 5 layers of magnets. The inner radius of the stainless steel outer sphere is 21 cm and its thickness is 5 mm. Blind holes are drilled and threaded along several meridians and parallels to receive M1.2 mm brass bolts acting as electrodes. In this article, results are presented for electric potentials measured along one meridian (on the left). The large holes at latitudes $-20°$, $10°$ and $\pm 40°$ receive interchangeable assemblies, which can be equipped with ultrasonic transducers. Magnetometers are placed at a latitude of $50°$, just above the outer sphere, in the laboratory frame. They measure the radial B_r and othoradial B_θ components of the magnetic field.

2.2 Electric potentials

We measure the electric potential at several points on the outer sphere. Blind holes are drilled in the 5 mm–thick stainless steel shell. The holes are 1 mm in diameter, and 4 mm–deep. They are threaded and equipped with 3 mm–long M1.2 mm brass bolts, on the head of which electrodes are soldered. Stainless steel is a poor electric conductor as compared to liquid sodium and thus it does not affect the dynamically generated electric potential, but it is a good enough electric conductor for the impedance of electrode pairs to be much smaller than that of the acquisition system. The measurements are acquired at 1 kHz with a PXI-6229 National Instruments board, after going through a simple anti–aliasing 215 Hz low–pass RC filter. As we focus here on the mean axisymmetric state, these data are time–averaged over time–windows ranging from 0.1 to 1 second, in order to remove fluctuations.

In this article, we present data for the difference in electric potential measured between electrodes placed along the same meridian. These electrodes are 10° apart and range from −45° to +45° in latitude as shown in figure 2. Assuming steady state, the difference in electric potential ΔV between two electrodes separated by a latitudinal angle $\Delta\theta$ is related to the azimuthal velocity U_φ of the liquid sodium by:

$$\frac{\Delta V}{a\Delta\theta} = U_\varphi B_r - \frac{j_\theta}{\sigma} \tag{1}$$

where B_r is the radial component of the magnetic field, j_θ is the θ-component of the electric current, and σ is the electric conductivity of liquid sodium.

In Nataf et al. (2006), we used the differences in electric potential to deduce the angular velocity of the liquid sodium flow beneath the Hartmann boundary layer. Indeed, assuming that the meridional electric currents vanish below that layer, equation 1 yields:

$$U_\varphi = \frac{\Delta V}{a\Delta\theta\, B_r}. \tag{2}$$

In this article, we will use the difference in electric potential measured at 40° latitude ($\Delta V_{40°}$) as a proxy of the actual velocity of the liquid sodium flow with respect to the outer sphere.

2.3 Ultrasonic Doppler velocimetry

Since liquid sodium is opaque, it is not possible to use optical methods to investigate the flow within the sphere. Instead, we use ultrasounds to probe the flow. Ultrasonic transducers are placed in removable assemblies on the outer sphere, and shoot a narrow beam of 4 MHz ultrasounds. The pulsed Doppler velocimetry technique is perfectly suited for retrieving profiles of the component of the flow velocity along the shooting line, as illustrated in Brito et al. (2001), Eckert & Gerbeth (2002), and Nataf et al. (2006).

While only radial profiles of the radial velocity were discussed in Nataf et al. (2006), we show here profiles of both the radial velocity and the azimuthal velocity, the latter being obtained with an assembly devised for shooting a beam at an angle of 24° away from radial. The axisymmetric angular frequency $\Delta f_{\text{fluid}}(s,z)$ of the fluid flow can be retrieved from the velocity $\mathcal{U}(d)$ measured along the shooting line, assuming that the meridional velocities are negligible compared to the azimuthal velocities. With our actual geometry, one gets:

$$\Delta f_{\text{fluid}}(s,z) = \frac{2.88}{2\pi}\frac{\mathcal{U}(d)}{a}, \tag{3}$$

where d is the distance along the shooting line, s the cylindrical radius, and z the height above the equatorial plane, which are related by:

$$z(d) = a \sin 10^\circ - 0.359\, d \tag{4}$$

$$s(d) = a \cos 10^\circ \sqrt{1 - 1.76\frac{d}{a} + 0.898 \left(\frac{d}{a}\right)^2} \tag{5}$$

As shown in figure 1, plotting z versus s for this beam yields an equivalent ray path, which corresponds to what would be seen for an axisymmetric flow. Tick marks have been drawn every 2 cm along the path. The minimum cylindrical radius reached is $s = 7.7$ cm, close to the radius of the inner sphere (7.4 cm), but it is attained some 4cm beneath the equator.

The Doppler technique relies upon ultrasonic energy backscattered by particles in the liquid. We did not add any particle in the liquid sodium. In liquid metals, it is often assumed that the backscattered echoes are due to floating oxides. It is interesting to note that we were able to record good profiles, even when the outer sphere was rotating at 14 Hz, implying centrifugal acceleration up to 180 times the acceleration due to gravity.

2.4 Induced magnetic field

The magnetic field is measured outside the sphere, in the laboratory frame. Both the radial B_r and the orthoradial B_θ components are measured with a "Giant Magnetoresistance" (GMR) chip. The two chips are mounted on a circuit protected by a stainless steel tube. The probe has been installed at a latitude of 50°, as close as possible to the rotating sphere: the distance to the center of the sphere is about 22 cm. The variation of temperature has a significant effect on the measurements. Temperature is thus measured close to the GMR magnetometers, and a linear correction scheme is applied. The acquisition rate is 2000 sample per second, but all data presented here have been moving–averaged over 3 seconds, since we are focusing on the average axisymmetric mean flow.

3 Dimensionless numbers

Relevant parameters and dimensionless numbers are given in table 1. As in all moderate–size liquid sodium experiments, the Joule dissipation time τ_J is relatively short. Since the imposed magnetic field is dipolar, its amplitude

is much larger near the inner sphere ($B = B_i$) than near the outer sphere ($B = B_o$). We therefore evaluate those numbers that depend on the strength of the magnetic field in these two regions. The Hartmann number Ha is large everywhere. The Lundquist number S is large near the inner sphere, implying that Alfvén waves can play a role in the dynamics, with typical velocities U_a ranging from 0.2 to 5 m/s.

Values of the Ekman number E are given for two typical values of the rotation rate f of the outer sphere. The DTS experiment has been designed for the study of the magnetostrophic regime, in which Lorentz forces and Coriolis forces are of similar amplitude. This is measured by the Elsasser number Λ, which ranges from 0.01 near the outer sphere (where Coriolis forces dominate) to nearly 10 near the inner sphere (where Lorentz forces dominate). For time–scales short compared to the magnetic diffusion time, a measure of the relative influence of the rotational and magnetic effects is given by the dimensionless number λ, the ratio of the Alfvén velocity to the inertial wave velocity (Fearn et al., 1988; Cardin et al., 2002), which is called the Lehnert number (Lehnert, 1954) by Jault (2007). The Lehnert number is small in planetary cores, and rotational effects are expected to dominate at short time–scales. In the DTS experiment, the Lehnert number is less than 1.

We estimate a typical velocity U from the magnitude of the differential rotation Δf of the inner sphere with respect to the outer sphere. The estimate is based on the tangential velocity at the equator of the inner sphere. We will see that, because the magnetic coupling between the magnetized inner sphere and the liquid sodium is strong, velocities in the fluid layer are typically even larger. This yields values of the magnetic Reynolds number Rm in excess of 40, while the Reynolds number Re lies in the range $10^5 - 10^6$. The interaction parameter N ranges from 0.01 near the outer sphere to 250 near the inner sphere, meaning that inertial effects only play a role near the outer boundary. Note that the Rossby number Ro is here simply defined as $\mathrm{Ro} = \Delta\Omega/\Omega = \Delta f/f$.

The DTS experiment thus enables us to explore an original parameter range, which covers some aspects of liquid core dynamics.

4 Results

4.1 A typical run

Figure 3 illustrates the data typically acquired during a 1600s-long run. The top graph shows the variation of f, the rotation frequency of the outer sphere, and Δf, that of the inner sphere with respect to the outer sphere. The outer

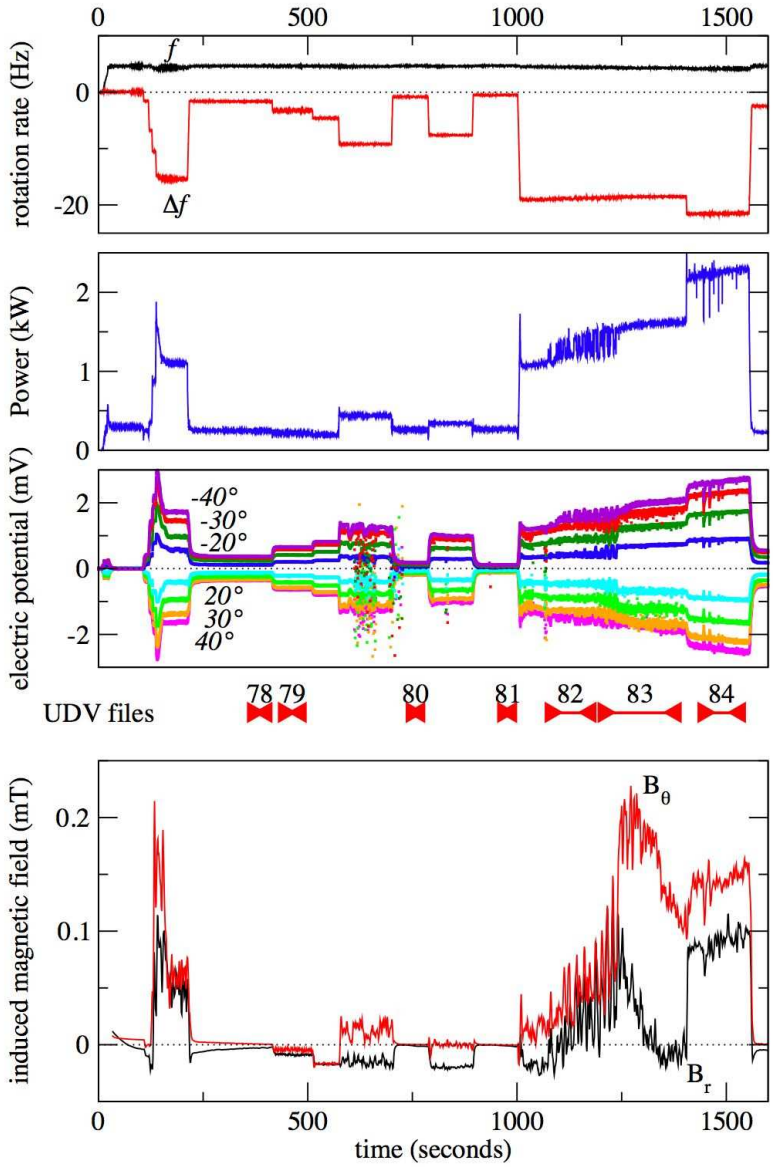

Fig. 3. An example of the data acquisition during an experimental run, as a function of time (in seconds). The top graph shows f, the rotation rate of the outer sphere, and Δf, the rotation rate of the inner sphere with respect to the outer sphere. The next graph below is the total power. The differences in electric potential recorded by the eight longitudinal electrode pairs (from $-40°$ to $40°$ latitude) is shown next. The time–log of the recorded ultrasonic Doppler files is shown below. The last graph below gives the induced magnetic field (in mT) recorded on the 50°-latitude magnetometer.

symbol	expression	units	value			
a	outer radius	cm	21			
b	inner radius	cm	7.4			
τ_J	$a^2/\pi^2\eta$	s	0.05			
			$B = B_i$		$B = B_o$	
Ha	$aB/\sqrt{\mu_0\rho\nu\eta}$		4400		210	
S	$aB/\eta\sqrt{\mu_0\rho}$		12		0.56	
U_a	$B/\sqrt{\mu_0\rho}$	m s^{-1}	5.1		0.2	
			$f = 5$Hz		$f = 15$Hz	
E	$\nu/\Omega a^2$		$4.7\ 10^{-7}$		$1.6\ 10^{-7}$	
			$B = B_i$	$B = B_o$	$B = B_i$	$B = B_o$
Λ	$\sigma B^2/\rho\Omega$		9.2	0.02	3.1	0.01
λ	$U_a/a\Omega$		0.77	0.04	0.26	0.01
			$\Delta f = 0.5$Hz		$\Delta f = 40$Hz	
U	$b\Delta\Omega$	m s^{-1}	0.23		18.6	
Rm	Ua/η		0.55		44	
Re	Ua/ν		$7\ 10^4$		$6\ 10^6$	
			$B = B_i$	$B = B_o$	$B = B_i$	$B = B_o$
N	$\sigma aB^2/\rho U$		262	0.06	3.1	0.01

Table 1
Typical values of the relevant parameters and dimensionless numbers for different imposed rotation frequencies $f = \Omega/2\pi$ of the outer sphere and differential rotation frequencies $\Delta f = \Delta\Omega/2\pi$ of the inner sphere. For the numbers that depend on the magnetic field strength, two values are given, the first one with $B = B_i = 0.175$ T at the equator of the inner sphere, the second one with $B = B_o = 0.008$ T at the equator of the outer sphere.

sphere is first set to a rotation rate of about 5 Hz, then several plateaux of different Δf are produced, down to Δf = -21.5 Hz. Here, they all correspond to counter–rotation. Some small fluctuations of the imposed rotation rates are observed ($\pm$3% max for Δf and $\pm$7% max for f). They are due to variations in the power demanded to the motors, as shown in the next graph below, which displays the total power of the motors, reaching 2.3 kW. Note the large power fluctuations ($\pm$22%) in the middle of the plateau for Δf = -19 Hz. The next graph gives the differences in electric potential ΔV recorded by the eight electrode pairs along a meridian. The highest signal reaches 3 mV. As expected from equation 2, the potential difference is largest at the highest latitude because B_r is largest there. Since Δf is negative, the electric

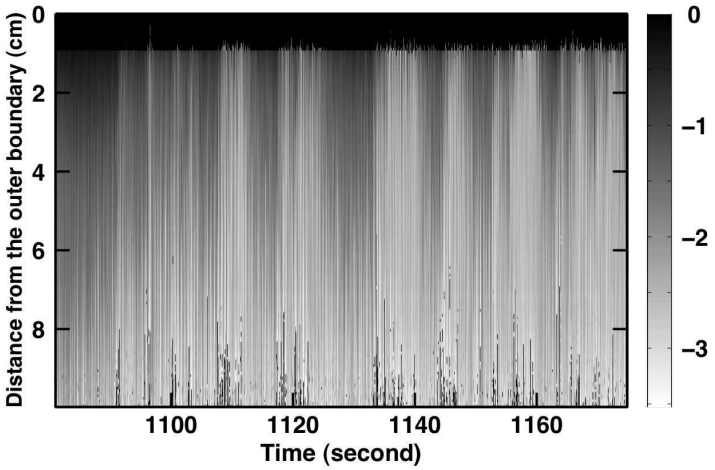

Fig. 4. An example of an ultrasonic Doppler velocity acquisition (file 82 in figure 3). The horizontal axis is time (in seconds) and the vertical axis is distance along the shooting line (in cm), here down to $d \simeq 10$ cm. The shades give the velocity value in m/s (scale on the right-hand side). Strong velocity fluctuations are observed.

potential differences are positive in the southern hemisphere and negative in the northern hemisphere (with our connection conventions). There is an almost perfect symmetry between the two hemispheres. Several ultrasonic Doppler velocity profiles are recorded during this sequence, as illustrated by the file log below. The last graph below shows the induced magnetic field measured at 50° latitude. The records have been time-averaged along a 3 seconds–window to remove the fluctuations linked with the rotation of the outer sphere, and the imposed dipole contribution has been removed. The plateaux are well identified, but large fluctuations are observed when Δf is large. The maximum amplitude of the induced magnetic field is 0.23 mT (2.4% of the imposed field at this position).

A typical ultrasonic Doppler velocity record is shown in figure 4. It corresponds to file 82 of the file log in figure 3, when time–oscillations are observed on all data. The spatiotemporal plot clearly shows these oscillations (a time–profile for one given depth d is also shown in a later figure (figure 13b)). The velocities are largest at the bottom of the figure, where the ultrasonic beam gets closest to the inner sphere for this record. Equation 5 gives the value of the cylindrical radius $s = 12.1$ cm. There, the velocity reaches -3.5 m/s. This large value is nevertheless much less than the imposed tangential velocity on the inner sphere (-8.7 m/s). For this file, the time–interval between profiles is 15 ms, and there are 128 shots per profile. Velocities cannot be measured in the first 1 cm of the records, due to strong reverberations in the assembly wall.

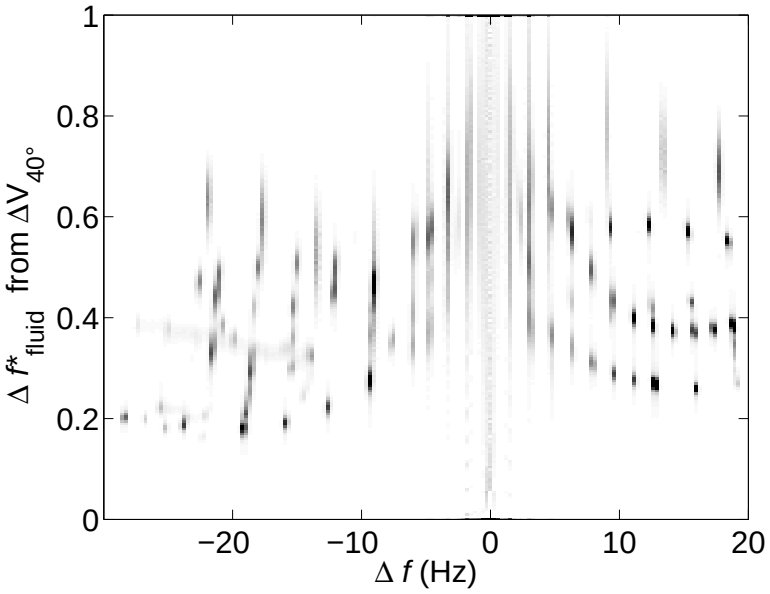

Fig. 5. A compilation of the variation of the normalized angular velocity of the liquid as a function of the imposed differential rotation rate Δf. The velocity of the outer sphere is $f \simeq 4.5$ Hz for all data shown. The shades give the proportion of data points that yield a given couple of values. Note that very different angular velocities are measured for a given Δf.

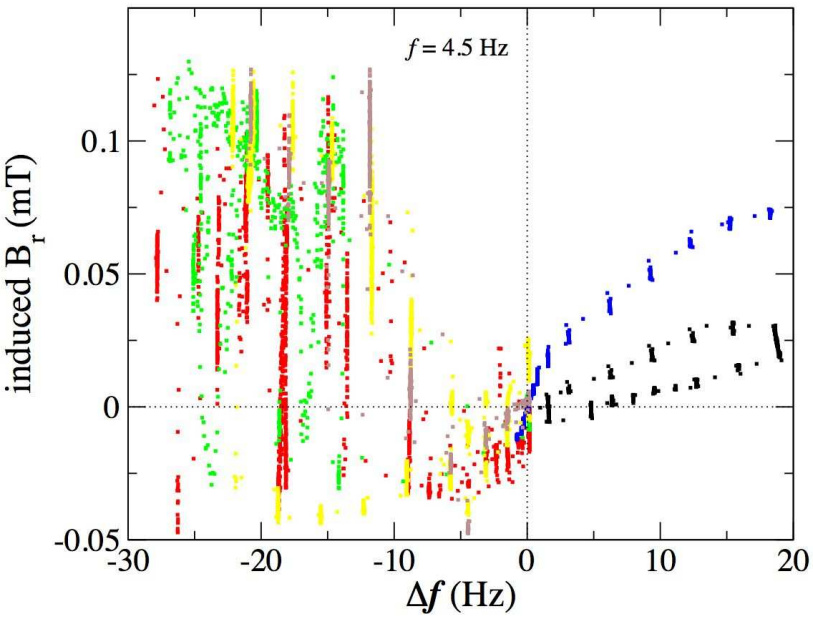

Fig. 6. A compilation of the variation of the radial component of the induced magnetic field as a function of the imposed differential rotation rate Δf. The velocity of the outer sphere is $f \simeq 4.5$ Hz for all data shown. The colors indicate different experimental runs. Note the large scatter of the data points, especially for negative Δf.

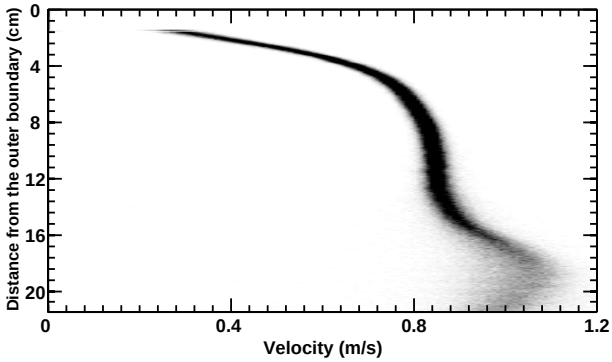

Fig. 7. Azimuthal velocity profile for $f = 4.7$ Hz and $\Delta f = 4.8$ Hz. The time–interval between profiles is 30 ms, and there are 128 shots per profile. Probability density function or histogram of the velocity as a function of distance along shot.

4.2 Evolution with the imposed differential rotation

Figure 5 shows the dimensionless angular frequencies $\Delta f^*_{\text{fluid}} = U_\varphi / 2\pi s \Delta f$ deduced from the electric potential differences measured at 40° latitude (according to equation 2), as a function of the imposed differential rotation Δf, for a given rotation rate $f \simeq 4.5$ Hz of the outer sphere. The figure is similar to figure 4 of Nataf et al. (2006), but data from several additional runs are included. The data points appear very scattered: for a given Δf, the dimensionless angular velocity can vary by up to a factor of 3. We think that this is due to variations in the electric coupling between liquid sodium and the inner copper sphere. The coupling between the rotating inner sphere and the liquid sodium depends on the electric currents that are induced in the sodium and loop in the copper inner sphere. A similar scatter is observed when plotting the induced magnetic field as a function of Δf (figure 6).

This scatter makes it difficult to draw robust conclusions about features such as super–rotation, but we will show in the next section that there is a linear relationship between the electric potential difference at 40° ($\Delta V_{40°}$) and the azimuthal velocities in the sodium actually measured with ultrasonic Doppler velocimetry. We will therefore use $\Delta V_{40°}$ as a proxy of the actual flow velocity, and we will see that several features of the flow become coherent when this proxy is used in place of Δf.

4.3 Azimuthal velocity profiles

Using Doppler ultrasonic velocimetry, we are able to measure azimuthal velocity of the liquid sodium flow. Figure 7 shows a profile of velocities measured along the shooting line for $f = 4.7$ Hz and $\Delta f = 4.8$ Hz. Equation 3 shows that the measured velocity component is proportional to the angular veloc-

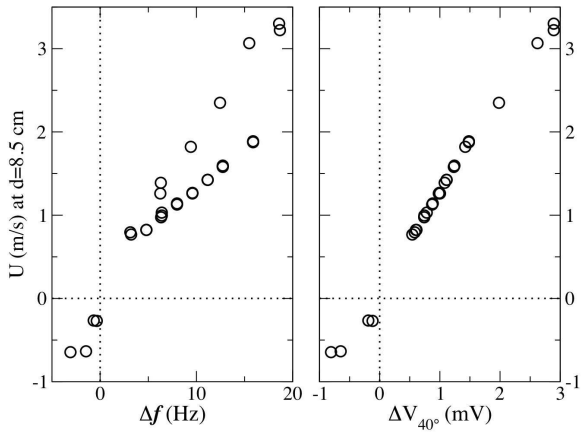

Fig. 8. Velocity (in m/s) at a distance of 8.5 cm along the shot line ($s \simeq 13.6$cm), as a function of Δf (left) and ΔV_{40° (right). The rotation rate of the outer sphere is $f \simeq 4.5$ Hz. The linear relation we get on the right shows that ΔV_{40° is a good proxy of the azimuthal velocity of the fluid at depth.

ity of the fluid. Actually, the plot is built from a 40 s–long record and the shades map the probability density function (*pdf*) of velocity versus distance (see Nataf et al. (2006)). In this regime, the flow is almost steady and the *pdf* is sharp. Velocity rises steadily from zero at the outer boundary (top of the graph) to reach a plateau of about 0.85 m/s. The velocity further increases to a bump at 1.05 m/s where the ultrasonic beam gets closest to the inner sphere ($d \simeq 18.8$ cm, $s \simeq 7.9$ cm). We interpret this bump as the signature of the magnetic wind, which is confined to the neighborhood of the inner sphere, where the magnetic field is largest. The plateau characterizes the region where the fluid is entrained at an almost uniform angular velocity by the magnetic wind, under the influence of the Coriolis force. This profile is typical of those measured when the outer sphere is rotating, and differs from those obtained when the outer sphere is at rest (see Brito et al. (2007)). For all available profiles, we pick the velocity measured at a distance of 8.5 cm (on the plateau, and about at mid–depth of the fluid layer, in the equatorial plane, according to figure 1) and plot it as a function of the corresponding Δf and ΔV_{40° (Figure 8). While the former plot displays a large scatter, all points align well when velocity is plotted against ΔV_{40°, illustrating the idea that the latter represents a good proxy of the effective velocity. From the regression line, we can translate ΔV_{40° into fluid velocity of fluid flow frequency at depth in the fluid. We obtain: $\Delta f^*_{\rm fluid}/\Delta V_{40^\circ} \simeq 2600$ Hz/V.

In figure 9, we have plotted all the profiles for $f \simeq 4.5$ Hz and positive Δf, divided by the corresponding ΔV_{40°. The horizontal scale has been chosen to provide the actual adimensional angular velocity for the reference case $\Delta f = 3.2$ Hz, according to equation 3. However, one should not consider this

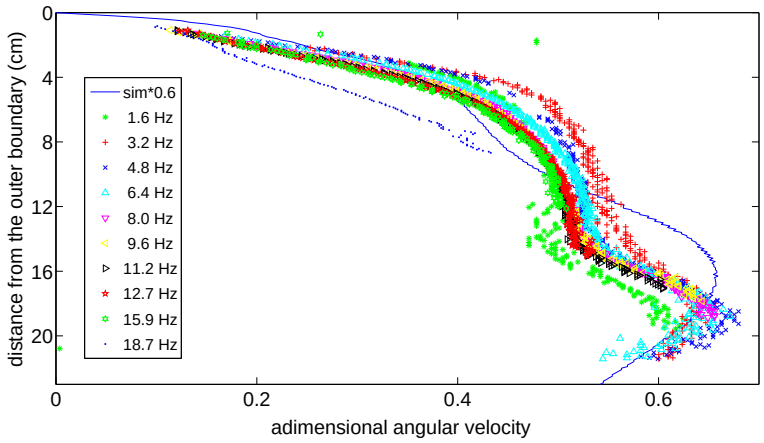

Fig. 9. A compilation of the azimuthal velocity profiles, normalized by ΔV_{40°, for $f \simeq 4.5$ Hz and for imposed Δf ranging from 1.6 to 18.7 Hz. The vertical scale has been chosen to give the actual adimensional angular velocity for the reference profile with $\Delta f = 3.2$ Hz. A synthetic profile, computed from the numerical simulation shown in figure 1 is drawn for comparison (solid line). Its amplitude is multiplied by 0.6.

scale as universal, since the actual coupling is very variable (see figure 5). We have also drawn a synthetic profile derived from the numerical simulation shown in figure 1, with an amplitude arbitrarily decreased by 40% in order to fall near the measured values. In a first approximation, all experimental profiles collapse on a single curve, showing that the normalization with ΔV_{40° is adequate. A closer look reveals that the rise of the velocity from the outer boundary is sharper when the forcing is weaker. In other words, the plateau of high angular velocity extends further towards the outer sphere for weak forcing. It seems that the relative size of the bump due to the magnetic wind above the plateau does not depend much upon the forcing. The comparison with the numerical profile suggests that the zone of strong magnetic wind is closer to the inner sphere in the experiments than in the simulation. We also note that the profile that corresponds to the highest differential rotation rate $\Delta f = 18.7$ Hz plots below the others and has a distinct kink near the outer boundary, which makes it look more alike the profiles obtained with $f = 0$.

4.4 Electric potentials

We showed in Nataf et al. (2006) that, when the outer sphere is at rest, the relative variation of electric potential differences (normalized to its value at 40°) with latitude is independent of the differential rotation rate Δf. The better data now available confirm this observation and further demonstrate that the latitudinal variation of potentials is close to, but significantly different from, the one expected for solid body rotation. Figure 10 gives the variation of

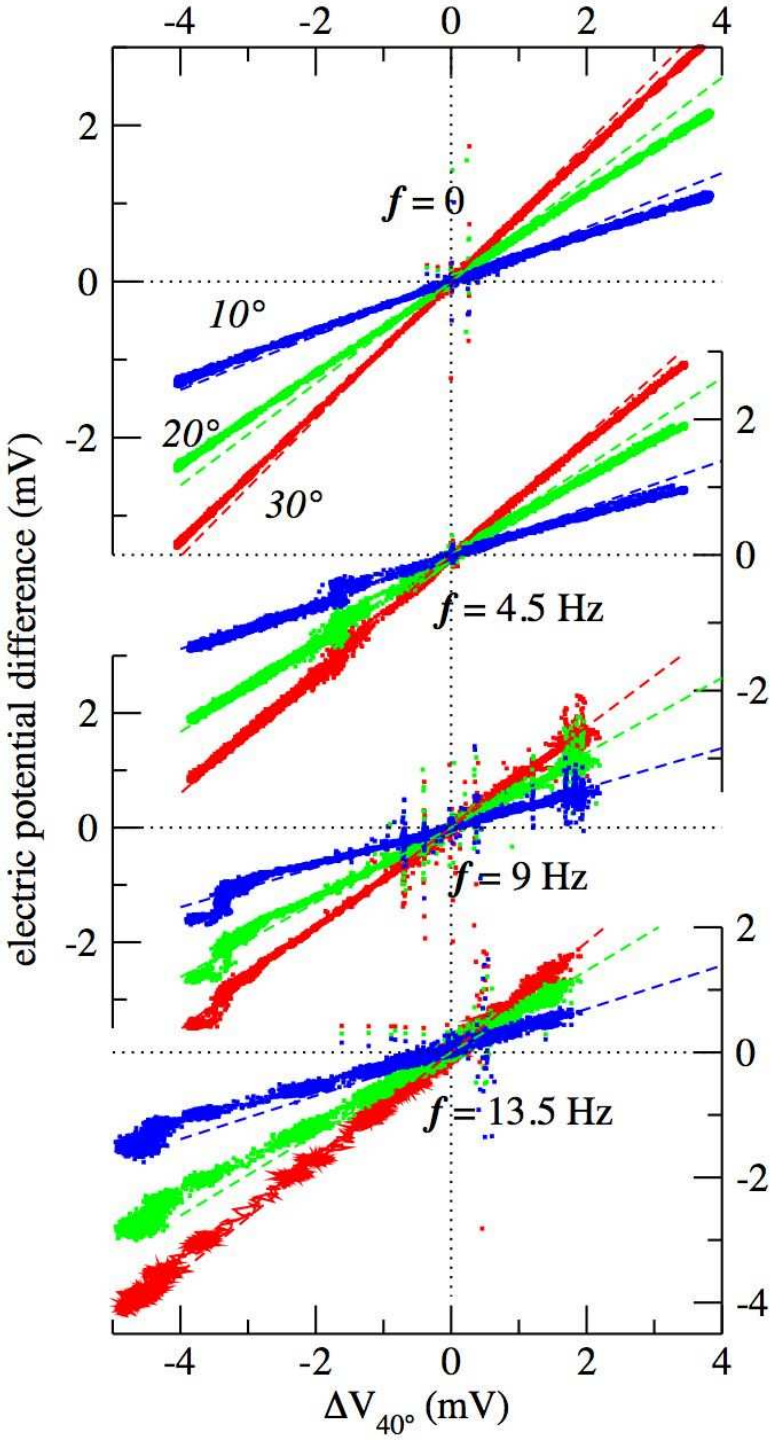

Fig. 10. A composite of electric potential differences for four different rotation rates f of the outer sphere. The electric potential difference measured at 10°, 20°, and 30° are plotted against that measured at 40°. The relation is almost linear, except for a kink observed around a negative value of $\Delta V_{40°}$, which moves towards more negative values when f increases. The dashed straight lines indicate the relationship one would get if the fluid was in solid body rotation. Scattered points in the bottom panels are due to electromagnetic noise.

electric potential differences ΔV at latitudes of 10°, 20° and 30° as a function of ΔV_{40°, for three different rotation rates of the outer sphere ($f = 4.5, 9$ and 13.5 Hz), and several different Δf (both positive and negative). The case with no rotation ($f = 0$) is included for reference. In all four cases, the data points align well, and fall not far from (but distinctly off) the straight lines calculated for solid body rotation (i.e., assuming U_φ proportional to s in equation 2). However, when the outer sphere is rotating, there is a distinct interval of ΔV_{40° that displays a peculiar behavior. It occurs around $\Delta V_{40^\circ} = -1.7$ mV for $f = 4.5$ Hz, -3.3 mV for $f = 9$ Hz, and -4.4 mV for $f = 13.5$ Hz. The kink means that, there, the variations in electric potentials are larger at low latitudes than at 40°. We will see below that the induced magnetic field also displays a very peculiar variation around the same ΔV_{40°.

4.5 Induced magnetic field

The induced magnetic field is measured outside the sphere, in the laboratory frame. The mean axisymmetric part of the induced field results from the interaction of the imposed axial dipolar magnetic field with the mean axisymmetric part of the meridional velocity field. The magnetometer signals are first averaged over 3 seconds, in order to remove the oscillatory part (which is discussed in another article (Schmitt et al., 2007)) and other magnetic perturbations. We then correct for temperature drift, by removing an empirical linear correction. In figure 11, both the radial B_r and orthoradial B_θ components are plotted as a function of ΔV_{40° for several different imposed rotation frequencies f of the outer sphere. We have included the $f = 0$ case for reference.

The first thing to note is the change of symmetry about $\Delta V_{40^\circ} = 0$ for small forcing : while the induced magnetic field is always positive when the outer sphere is at rest, we find that the induced field has the sign of ΔV_{40° (or Δf) when the outer sphere is rotating. This can be directly related to the sense of the meridional circulation. When the outer sphere is at rest, the flow is always centrifugal in the equatorial plane, irrespective of the sign of Δf. When the outer sphere is rotating, the sense of the mass flux through the outer viscous boundary layer is governed by the sign of the differential rotation between the fluid and the outer sphere (as for Ekman pumping). When $\Delta f/f$ is negative and small enough, the mass flux out of the boundary layer is thus centripetal at the equator.

In that same regime, we also note that the induced magnetic field is weaker when the outer sphere is rotating : the meridional circulation violates the Proudman–Taylor constraint and therefore decreases as the Ekman number decreases (see figure 6 of Hollerbach et al. (2007)).

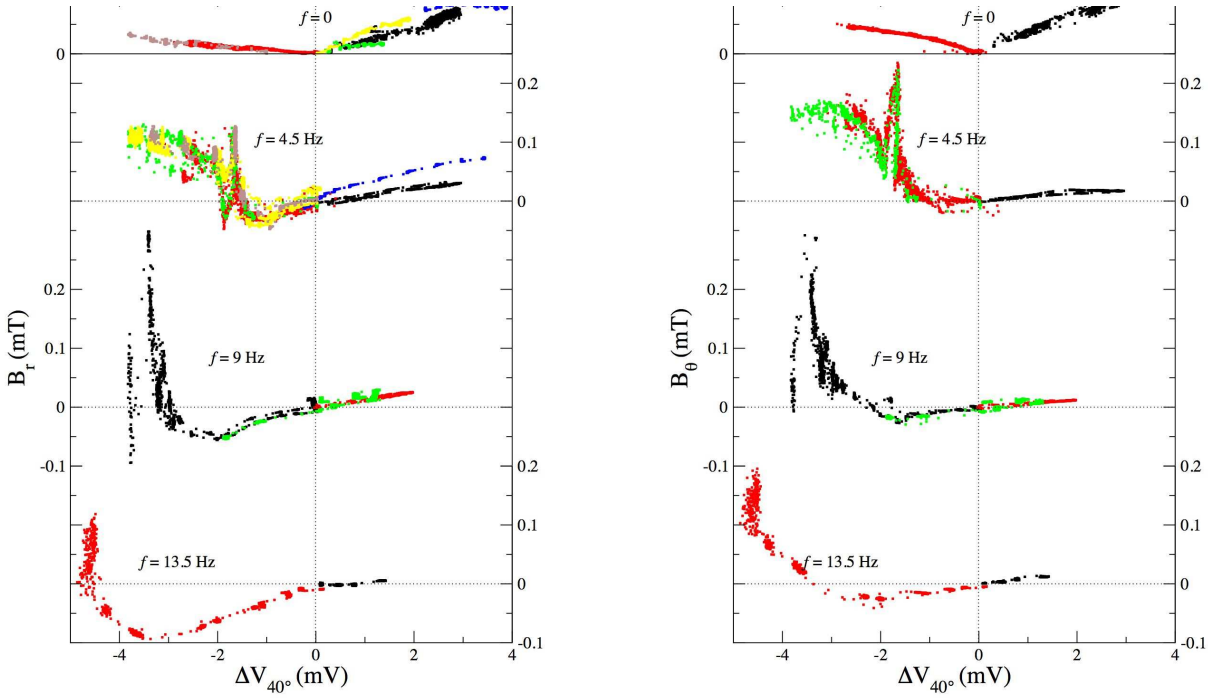

Fig. 11. A composite of the induced magnetic field as a function of ΔV_{40°, for four different rotation frequencies f of the outer sphere. Radial component on the left, and orthoradial component on the right. Note the symmetry change around the origin ($\Delta f \simeq 0$) between the case without rotation ($f = 0$) and the other cases. A striking peak is observed for a particular value of Δf in the counterrotating regime ($\Delta V_{40^\circ} < 0$). The colors correspond to different runs.

However, the most interesting feature of the curves shown in figure 11 is the distinctive narrow peak observed at negative Δf (here negative ΔV_{40°). The peak occurs for a value of ΔV_{40° that moves toward more negative values as f increases. In fact, the occurrence of the peak corresponds to the transition between two different regimes, which was invoked when discussing figure 10. We stress that it is because we plot the induced magnetic field as a function of ΔV_{40° rather than Δf that we obtain a well defined and reproducible peak (compare with figure 6). The peak happens as the flow evolves from centripetal to centrifugal in the equatorial plane, as the effect of differential rotation takes over the effect of global rotation. Our interpretation is that, in a narrow window of ΔV_{40°, the antagonistic effects of the rotation of the outer and inner spheres drive the liquid in a state that shows almost no rotation with respect to the laboratory frame. The constraint of rotation then vanishes, and a vigorous meridional circulation is allowed, resulting in an enhanced induced

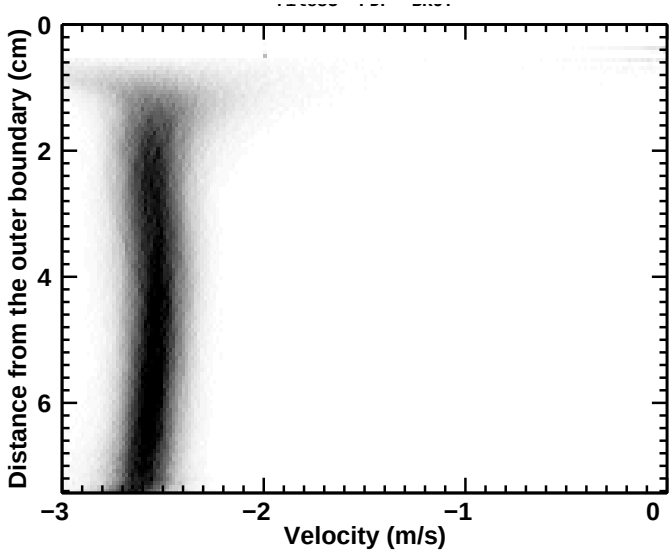

Fig. 12. A profile (*pdf*) of the angular velocity of the fluid for $f = 4.2$Hz and $\Delta f = -18.2$Hz, for which $\Delta V_{40^\circ} = -1.7$mV. This value corresponds to the peak observed for the induced magnetic field.

magnetic field.

Some support for this interpretation is given by a direct measurement of the azimuthal velocity using the ultrasonic Doppler technique. As shown in figure 12, a peculiar profile is measured close to the B peak. An almost uniform angular velocity is measured (down to $d \simeq 7.4$ cm, i.e. at mid–depth of the fluid shell). Using equation 3, we find a fluid rotation frequency of -5.7 Hz on this plateau. Since the ultrasonic probe is installed in the rotating sphere, the angular velocity with respect to the laboratory frame is obtained by adding the angular velocity of the outer sphere. The resulting angular velocity is then -5.7 + 4.2 = -1.5 Hz, which is small but non zero. The above scenario is probably too simple, and the variation of the induced magnetic field calls for a more sophisticated interpretation. For example, the B_r and B_θ records of figure 3 show that the "centrifugal" regime is announced by a strong rise of B_θ, while B_r starts decreasing instead.

4.6 Transition scenarios

The counter–rotative situation is characterized by two different regimes: for small negative Rossby numbers, the flow is influenced by Ekman–like pumping on the outer sphere, resulting in centripetal velocities at the equator; for large negative Rossby numbers, the flow is dominated by centrifugal velocities at the equator, forced by the rotation of the inner sphere. The transition between these two regimes occurs in a small interval of ΔV_{40°. In several instances, this

transition occurred spontaneously, without changing the inner sphere differential rotation rate Δf, but the time–evolution of the flow during the transition can be complex.

Two different transition scenarios have been identified, which we document here. The first transition scenario is oscillatory and the flow remains almost symmetric with respect to the equatorial plane, while the second one is sudden and the flow is strongly asymmetric.

4.6.1 Oscillatory transition with an equatorially symmetric flow

This transition is visible in the example run of figure 3: while the imposed differential rotation rate of the inner sphere Δf is kept fixed around -19 Hz, strong oscillations appear and dominate all signals (power, electric potentials, velocities, magnetic field). A close-up of these oscillations is given in figure 13. The beginning of the sequence is in the centripetal regime ($\Delta V_{40^\circ} < 1.7$mV), while the end is in the centrifugal regime ($\Delta V_{40^\circ} > 1.7$mV). A dozen of irregular oscillations with a period of about 10 seconds are observed. Figure 13a shows the electric potential differences at four different latitudes. The opposite of the southern hemisphere signals are also plotted. The oscillations appear to be nearly in phase at all latitudes. The signals of the two hemispheres superpose nicely, indicating that the oscillations are symmetric with respect to the equatorial plane. The oscillations seem to spread from high to low latitudes, and the amplitude of the oscillations tends to increase with time at the lowest latitude, until the final jump. In a further blow–up, figure 13b compares the variations of the electric potential at 40° with those of the induced radial magnetic field and of the azimuthal velocities at $d \simeq 5.9$cm ($s \simeq 15.7$ cm), measured by ultrasonic velocimetry. The vertical scale relates to the latter, while the other curves have been scaled up arbitrarily. The first thing to note is the clear correlation between the three kinds of measurements. Note that the ratio of the amplitude of the oscillations of ΔV_{40° to those of $\mathcal{U}$ is about four times smaller than would be predicted from the linear relation of figure 8. This is an indication that they are not related to variations in the electric coupling between the inner sphere and liquid sodium, but rather have a distinct dynamical origin.

4.6.2 Sudden transition with an equatorially asymmetric flow

A different and spectacular transition was observed during another run, also for $f = 4.5$ Hz. Shortly after an increase of the amplitude of the imposed differential rotation rate Δf from -18.8 to -21.9 Hz, the electric potential differences in the northern hemisphere started increasing steadily, while nothing was changing in the southern hemisphere. After about 10 seconds, the electric

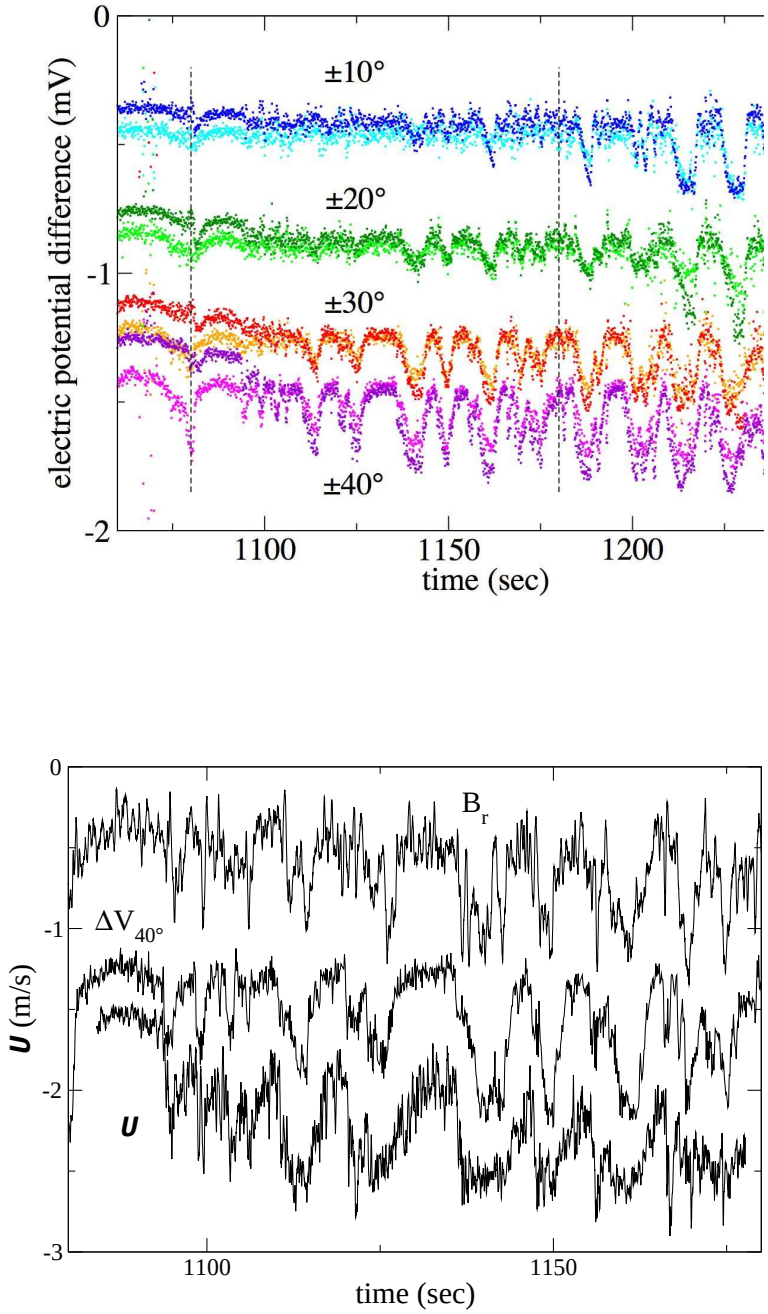

Fig. 13. Transition between the centripetal and centrifugal regimes: the oscillatory scenario with an equatorially symmetric flow. (a) electric potential differences recorded at the various latitudes in the northern and southern hemispheres. The oscillations seem to spread from high to low latitudes before the transition takes place. (b) comparison between signals of different origin for the time–window between the two vertical lines of the previous figure. The oscillations seen in the electric potentials are also clear in the records of the Doppler velocity $\mathcal{U}$ and induced magnetic field B_r. The vertical scale only applies for $\mathcal{U}$.

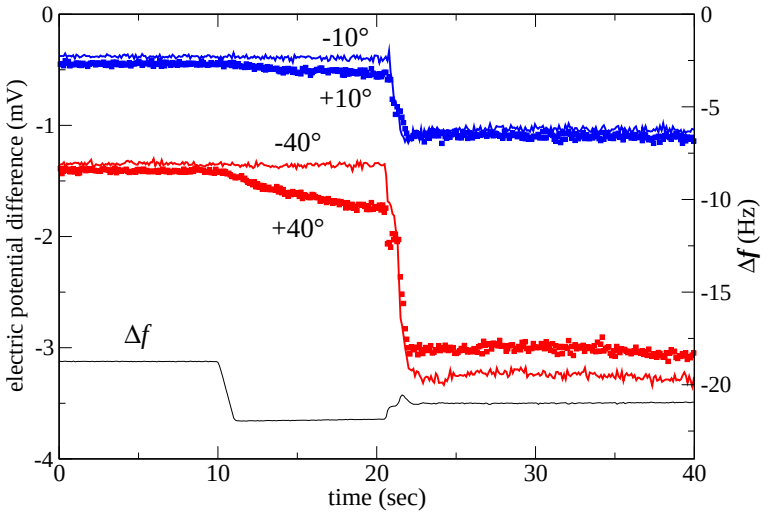

Fig. 14. Transition between the centripetal and centrifugal regimes: the sudden scenario with an equatorially asymmetric flow. The electric potential differences measured at $\pm 10°$ and $\pm 40°$ are plotted as a function of time. The lower curve is the imposed differential rotation frequency Δf (right hand scale). A sudden rise of the electric potentials is observed some 10 seconds after Δf was brought from -18.8 to -21.9 Hz. The transition appears to start in the northern hemisphere before it accelerates sharply in both hemispheres. The increased dissipation in the final state is responsible for the observed readjustment of Δf at the jump.

potential differences surged in the southern hemisphere, entraining those of the northern hemisphere. In the end, the differences in electric potentials had increased by more than a factor of 2. Figure 14 illustrates this transition, with the signals at 10° and 40° in both hemispheres. Note that, in this case, it is likely that an increase in the electric coupling between the inner sphere and the liquid sodium was responsible for the sudden transition.

5 Discussion and conclusions

The magnetostrophic regime at small Rossby numbers is characterized by a low level of turbulence. Most of the energy is in the axisymmetric mean flow described in this article. The meridional circulation has the symmetry of Ekman pumping: centrifugal at the equator for $\mathrm{Ro} > 0$ and centripetal for $\mathrm{Ro} < 0$. Its magnitude is at least one order of magnitude smaller than the azimuthal one. As for the Ekman pumping, the ratio between the meridional and azimuthal velocities decreases when f increases. Waves are observed in this regime, and will be described in a forthcoming article (Schmitt et al., 2007).

Radial profiles of the angular velocity of the flow have been obtained, using

ultrasonic Doppler velocimetry. They reveal a region where magnetic wind is present, near the inner sphere, where the magnetic field is largest. Farther away, the fluid is entrained at a nearly uniform angular velocity, under the effect of the Coriolis force.

In Nataf et al. (2006), there were hints that different flows could be obtained for the same imposed rotation rates f and Δf. Our new data confirm this trend. We speculate that this behavior is due to variations in the electric coupling between liquid sodium and the copper inner sphere, under the effect of electrowetting feedback. It is thus difficult to relate the observed signals to the imposed Δf, as we would like to do in order to study the possibility for the magnetic wind to induce super–rotation of the fluid as in Dormy et al. (1998). However, we find that most results can be cast in a common frame if we use ΔV_{40°, the electric potential difference at latitude 40°, as a proxy of the actual azimuthal velocity, in place of Δf. Recipes for a good electrowetting specify that the sodium should be kept in contact with the copper inner sphere at a temperature of 150°C during 3 days. A scenario for achieving this in DTS is under study.

In the counter–rotating case, the centripetal circulation at the equator, which characterizes the small Rossby number regime, transforms into a centrifugal circulation at the equator as the Rossby number increases. The transition between the two regimes occurs over a narrow interval of ΔV_{40°, and is marked by a peak of the induced magnetic field. This happens where the effective velocity of the fluid is such that it almost cancels that of the outer sphere, as seen in the laboratory frame.

The transition between the centripetal and the centrifugal regimes deserves a specific discussion in the context of the preparation of experimental dynamos. In Cardin et al. (2002), we evaluated the possibility to run a dynamo where the forcing is a rotating spherical Couette flow. Such a dynamo would run in the magnetostrophic regime, expected for planetary cores, and it would be of the $\alpha\omega$-type, displaying large azimuthal magnetic fields. The critical magnetic Reynolds number Rm_c for these robust dynamos appears however to be high (Schaeffer & Cardin, 2006). In contrast, the mean flow in other experiments (Peffley et al., 2000; Ravelet et al., 2005; Bayliss et al., 2007) is tuned to be close to an axi–symmetric flow of the Dudley & James (1989) family, with a strong meridional circulation, yielding an α^2-dynamo, and moderate Rm_c (Kumar & Roberts, 1975; Dudley & James, 1989). Indeed, there is an optimum ratio of meridional to azimuthal velocities that yield a minimum Rm_c (Ravelet et al., 2005; Bayliss et al., 2007). Here, we find that, in a rapidly rotating spherical Couette flow, the meridional velocities are at least one order of magnitude smaller than the azimuthal velocities. However, in the narrow window that corresponds to the transition from the centripetal regime to the centrifugal regime, the magnitude of the meridional circulation becomes comparable

to the azimuthal one. We suggest that the value of the magnetic Reynolds number for the onset of dynamo action will be minimum around this transition. Numerical evidence in support of this suggestion will be presented in a forthcoming article (Cardin & Jault, 2007). A rotating spherical Couette flow dynamo experiment should thus make it possible to observe the transition from an α^2–type to an $\alpha\omega$–type dynamo.

Concerning the time evolution of the transition from a centripetal to a centrifugal meridional circulation at $\mathrm{Ro} < 0$, two distinct scenarios have been documented: an oscillatory behavior with an equatorially symmetric flow or a sudden jump with a strongly asymmetric flow. Both cases deserve a more detailed analysis, which is currently under way.

6 Acknowledgments

We thank Jean-Paul Masson and Patrick La Rizza for their skillful technical assistance, and Alexandre Fournier for useful discussions. The *DTS* project is supported by Fonds National de la Science, Institut National des Sciences de l'Univers, Centre National de la Recherche Scientifique, Région Rhône-Alpes and Université Joseph Fourier.

References

Bayliss, R. A., Forest, C. B., Nornberg, M. D., Spence, E. J., & Terry, P. W., 2007, Numerical simulations of current generation and dynamo excitation in a mechanically forced turbulent flow, *Physical Review E*, **75**(2), 026303–+.

Braginsky, S. I. & Meytlis, V. P., 1990, Local turbulence in the Earth's core, *Geophysical and Astrophysical Fluid Dynamics*, **55**, 71–87.

Brito, D., Nataf, H.-C., Cardin, P., Aubert, J., & Masson, J.-P., 2001, Ultrasonic Doppler velocimetry in liquid gallium, *Experiments in Fluids*, **31**, 653–663.

Brito, D., Alboussière, T., Cardin, P., Gagnière, N., Jault, D., Nataf, H.-C., & Schmitt, D., 2007, Experimental measurements of the mean flow in a magnetohydrodynamic spherical Couette flow, *in preparation*.

Buffett, B. A., 2003, A comparison of subgrid-scale models for large-eddy simulations of convection in the Earth's core, *Geophysical Journal International*, **153**, 753–765.

Cardin, P. & Jault, 2007, Spherical Couette flows in presence of an axial magnetic dipole, *in preparation*.

Cardin, P., Brito, D., Jault, D., Nataf, H.-C., & Masson, J.-P., 2002, Towards A Rapidly Rotating Liquid Sodium Dynamo Experiment, *Magnetohydrodynamics*, **38**, 177–189.

Dormy, E., Cardin, P., & Jault, D., 1998, MHD flow in a slightly differentially rotating spherical shell, with conducting inner core, in a dipolar magnetic field, *Earth and Planetary Science Letters*, **160**, 15–30.

Dormy, E., Jault, D., & Soward, A. M., 2002, A super–rotating shear layer in magnetohydrodynamic spherical Couette flow, *J. Fluid Mech.*, **452**, 263–291.

Dudley, M. L. & James, R. W., 1989, Time-dependent kinematic dynamos with stationary flows, *Royal Society of London Proceedings Series A*, **425**, 407–429.

Eckert, S. & Gerbeth, G., 2002, Velocity measurements in liquid sodium by means of ultrasound Doppler velocimetry, *Experiments in Fluids*, **32**, 542–546.

Fearn, D. R., Roberts, P. H., & Soward, A. M., 1988, Convection, stability and the dynamo, in *Energy Stability and Convection*, edited by G. P. Galdi & B. Straughan, pp. 60–324, Longman scientific and technical Harlow.

Hollerbach, R., 1994, Magnetohydrodynamic Ekman and Stewartson layers in a rotating spherical shell, *Proc. R. Soc. Lond. A*, **444**, 333–346.

Hollerbach, R., 2000, Magnetohydrodynamic flows in spherical shells, in *LNP Vol. 549: Physics of Rotating Fluids*, edited by C. Egbers & G. Pfister, pp. 295–+.

Hollerbach, R., Canet, E., & Fournier, A., 2007, Spherical Couette flow in a dipolar magnetic field, *ArXiv Physics e-prints*.

Jault, D., 2007, Axial invariance of rapidly varying diffusionless motions in the Earth's core interior, *Physics of the Earth and Planetary Interiors*, p. to be submitted.

Kelley, D. H., Triana, S. A., Zimmerman, D. S., Brawn, B., Lathrop, D. P., & Martin, D. H., 2006, Driven inertial waves in spherical Couette flow, *Chaos*, **16**, 1105–+.

Kelley, D. H., Triana, S. A., Zimmerman, D. S., Tilgner, A., & Lathrop, D. P., 2007, Inertial waves driven by differential rotation in a planetary geometry, *to be submitted*.

Kleeorin, N., Rogachevskii, I., Ruzmaikin, A., Soward, A. M., & Starchenko, S. V., 1997, Axisymmetric flow between differentially rotating spheres in a dipole field, *J. Fluid Mech.*, **344**, 213–244.

Kumar, S. & Roberts, P. H., 1975, A Three-Dimensional Kinematic Dynamo, *Royal Society of London Proceedings Series A*, **344**, 235–258.

Lehnert, B., 1954, Magnetohydrodynamic Waves Under the Action of the Coriolis Force., *Astrophysical Journal*, **119**, 647–+.

Matsui, H. & Buffett, B. A., 2006, A test of sub-grid scale models for dynamo simulations in a rotating spherical shell, *AGU Fall Meeting Abstracts*, pp. A1027+.

Nataf, H.-C., Alboussière, T., Brito, D., Cardin, P., Gagnière, N., Jault, D.,

Masson, J.-P., & Schmitt, D., 2006, Experimental study of super-rotation in a magnetostrophic spherical Couette flow, *Geophysical and Astrophysical Fluid Dynamics*, **100**, 281–298.

Peffley, N. L., Goumilevski, A. G., Cawthrone, A. B., & Lathrop, D. P., 2000, Characterization of experimental dynamos, *Geophysical Journal International*, **142**, 52–58.

Ravelet, F., Chiffaudel, A., Daviaud, F., & Léorat, J., 2005, Toward an experimental von Kármán dynamo: Numerical studies for an optimized design, *Physics of Fluids*, **17**, 7104–+.

Schaeffer, N. & Cardin, P., 2006, Quasi-geostrophic kinematic dynamos at low magnetic Prandtl number, *Earth and Planetary Science Letters*, **245**, 595–604.

Schmitt, D., Alboussière, T., Brito, D., Cardin, P., Gagnière, N., Jault, D., & Nataf, H.-C., 2007, Rotating spherical Couette flow in a dipolar magnetic field: Experimental evidence of hydromagnetic waves, *Journal of Fluid Mechanics*, p. to be submitted.

Sisan, D. R., Mujica, N., Tillotson, W. A., Huang, Y.-M., Dorland, W., Hassam, A. B., Antonsen, T. M., & Lathrop, D. P., 2004, Experimental Observation and Characterization of the Magnetorotational Instability, *Physical Review Letters*, **93**(11), 114502–+.

St. Pierre, M. G., 1996, On the local nature of turbulence in Earth's outer core, *Geophysical and Astrophysical Fluid Dynamics*, **83**, 293–306.

Starchenko, S. V., 1998, Magnetohydrodynamic flow between insulating shells rotating in strong potential field, *Physics of Fluids*, **10**, 2412–2420.